of all transcription), more than half of nuclear poly A– sequences are derived from intronic regions (Table 1). Clearly, some of these poly A– sequences are introns of spliced coding gene transcripts and may or may not have further biological function once removed from the primary transcripts. However, in the cytosol, the amount of exclusively poly A– sequences is still twice as great as poly A+ sequences (Table 1A), which indicates that there are processed mature poly A– transcripts.

Finally, a total of 36.9% of transcribed sequences are detected as poly A– and poly A+ (Table 1B). These bimorphic sequences are distributed between the two subcellular compartments. It is important to note that detected bimorphic transcribed sequences may be two different transcripts, because transfrags do not identify the strand or specific full-length transcript. However, the presence of such a large proportion of bimorphic transcribed sequences suggests that novel regulatory mechanisms may be involved in the identification of transcripts whose polyadenylation states are altered as a means of regulation. Many of the detected bimorphic sequences are well-characterized coding genes found on the 10 analyzed chromosomes (table S3).

The observations derived from these studies provide some pause as to the state of our understanding concerning where and how the information from the human genome is organized. Many of these and other published observations indicate that our current understanding of the repertoire of transcripts made by the human genome is still evolving. A critical question that applies to both poly A– and poly A+ TUFs centers on the biological functions of these transcripts. Biochemical and genetic experimental approaches are currently being used to answer this question. Until these experiments are completed, systematic identification, mapping, and characterization of as many types of TUFs as possible will assist in understanding and appreciating the complexity of the human transcriptome.

References and Notes

1. E. S. Lander *et al.*, *Nature* **409**, 860 (2001).
2. J. C. Venter *et al.*, *Science* **291**, 1304 (2001).
3. P. Kapranov *et al.*, *Science* **296**, 916 (2002).
4. D. Kampa *et al.*, *Genome Res.* **14**, 331 (2004).
5. S. Cawley *et al.*, *Cell* **116**, 499 (2004).
6. J. L. Rinn *et al.*, *Genes Dev.* **17**, 529 (2003).
7. R. Yelin *et al.*, *Nat. Biotechnol.* **21**, 379 (2003).
8. R. Martone *et al.*, *Proc. Natl. Acad. Sci. U.S.A.* **100**, 12247 (2003).
9. The ENCODE Project Consortium, *Science* **306**, 636 (2004).
10. M. L. Birnstiel, M. Busslinger, K. Strub, *Cell* **41**, 349 (1985).
11. C. Milcarek, R. Price, S. Penman, *Cell* **3**, 1 (1974).
12. M. Salditt-Georgieff, M. M. Harpold, M. C. Wilsone, J. E. Darnell, *Mol. Cell. Biol.* **1**, 177 (1981).
13. P. K. Katinakis, A. Slater, R. H. Burdon, *FEBS Lett.* **116**, 1 (1980).
14. P. Bertone *et al.*, *Science* **306**, 2242 (2004).
15. Materials and methods are available as supporting material on *Science* Online.
16. D. Karolchik *et al.*, *Nucleic Acids Res.* **31**, 51 (2003).
17. W. J. Kent *et al.*, *Genome Res.* **12**, 996 (2002).
18. International Human Genome Sequencing Consortium, *Nature* **431**, 931 (2004).
19. J. Chen *et al.*, *Proc. Natl. Acad. Sci. U.S.A.* **99**, 12257 (2002).
20. Y. Kawabe *et al.*, *J. Biol. Chem.* **276**, 20364 (2001).
21. R. C. Inhorn, D. M. Tollefsen, *Biochem. Biophys. Res. Commun.* **137**, 431 (1986).
22. D. D. Shoemaker *et al.*, *Nature* **409**, 922 (2001).
23. K. Yamada *et al.*, *Science* **302**, 842 (2003).
24. V. Stolc *et al.*, *Science* **306**, 655 (2004).
25. Y. Okazaki *et al.*, *Nature* **420**, 563 (2002).
26. T. Ota *et al.*, *Nat. Genet.* **36**, 40 (2004).
27. The Mammalian Gene Collection Project Team, *Genome Res.* **14**, 2121 (2004).
28. T. Imanishi *et al.*, *PLoS Biol.* **2**, 856 (2004).
29. M. Seki *et al.*, *J. Exp. Bot.* **55**, 213 (2004).
30. S. Saha *et al.*, *Nat. Biotechnol.* **20**, 508 (2002).
31. H. Bono *et al.*, *Genome Res.* **13**, 1318 (2003).
32. A. Peragine, M. Yoshikawa, G. Wu, H. L. Albrecht, R. S. Poethig, *Genes Dev.* **18**, 2368 (2004).
33. F. Vazquez *et al.*, *Mol. Cell* **16**, 69 (2004).
34. M. Edmonds, M. G. Caramela, *J. Biol. Chem.* **244**, 1314 (1969).
35. B. J. Snider, M. Morrison-Bogorad, *Brain Res. Brain Res. Rev.* **17**, 263 (1992).
36. T. E. Geoghegan, G. E. Sonenshein, G. Brawerman, *Biochemistry* **17**, 4200 (1978).

37. The authors thank S. Cawley, C. Schaefer, and J. Manak for helpful discussions; M. Mittmann and D. Le for design of photolithographic masks; D. Bartell for software; R. Wheeler for assistance on the annotation database; H. Caley, H. Gorrell, and B. Wong for database support; J. Stevens for administrative support; and K. Kong for manuscript editing and management assistance. All sequenced transcripts have been submitted to GenBank (accession numbers: AY927468 to AY927642). The supplemental materials, feature intensity (CEL) files, graph file, transfrag, and RACE data are available at http://transcriptome.affymetrix.com/publication/transcriptome_10chromosomes and http://cgap.nci.nih.gov/Info/2005.1. Visual representations of the graph and transfrag data are available at http://genome.ucsc.edu/cgi-bin/hgTracks. This project has been funded in part with federal funds from the National Cancer Institute, National Institutes of Health, under contract N01-C0-12400, and by Affymetrix, Inc. The content of this publication does not necessarily reflect the views or policies of the Department of Health and Human Services, nor does mention of trade names, commercial products, or organizations imply endorsement by the U.S. government.

Supporting Online Material
www.sciencemag.org/cgi/content/full/1108625/DC1
Materials and Methods
Figs. S1 to S10
Tables S1 and S2
References

13 December 2004; accepted 15 March 2005
Published online 24 March 2005;
10.1126/science.1108625
Include this information when citing this paper.

REPORTS

Wet Electrons at the $H_2O/TiO_2(110)$ Surface

Ken Onda,[1] Bin Li,[1] Jin Zhao,[1] Kenneth D. Jordan,[2] Jinlong Yang,[3] Hrvoje Petek[1]*

At interfaces of metal oxide and water, partially hydrated or "wet-electron" states represent the lowest energy pathway for electron transfer. We studied the photoinduced electron transfer at the $H_2O/TiO_2(110)$ interface by means of time-resolved two-photon photoemission spectroscopy and electronic structure theory. At ~1-monolayer coverage of water on partially hydroxylated TiO_2 surfaces, we found an unoccupied electronic state 2.4 electron volts above the Fermi level. Density functional theory shows this to be a wet-electron state analogous to that reported in water clusters and which is distinct from hydrated electrons observed on water-covered metal surfaces. The decay of electrons from the wet-electron state to the conduction band of TiO_2 occurs in ≤15 femtoseconds.

The transport of charge through metal-oxide/hydrous phases is crucial to physical and chemical phenomena in many fields of science and technology, including geochemistry, electrochemistry, corrosion, photocatalysis, sensors, and electronic devices (*1*). When exposed to water vapor, metal oxides are partially hydroxylated and covered with up to several monolayers of H_2O. Interactions of the surface acidic metal and basic O ions, respectively, with the O and H atoms of water impose a two-dimensional (2D) order on the hydrated oxide interface (Fig. 1C). In a redox process, electrons must breach this unique 2D environment before they attain fully 3D hydrated Kevan structure proposed for liquid water, in which six tetrahedrally disposed water molecules point one of their H atoms into the excess electron cloud (*2*, *3*). Similar 2D environments, dubbed "wet-electron" states (*4*), in which the "dangling"—i.e., non–hydrogen bonded—H atoms bind and partially hydrate electrons on surfaces of small water clusters, have recently been predicted by theory and discovered in experiments (*5*–*9*). The electronic structure of wet-electron states at the metal-oxide/water interfaces and the dynamics of charge flow that they mediate have not been explored.

The study of the interfacial charge-transfer dynamics at H_2O/TiO_2 surfaces is of particular interest (*10*–*13*) because photoexcited carriers decompose adsorbed molecules (*14*, *15*), drive photovoltaic cells (*16*), and modify the surface wetting properties (*17*). Photoexcitation of electron-hole pairs across the 3.05-eV band gap of TiO_2 initiates a chain of redox reactions spanning subpicosecond to hour time scales (*18*, *19*). Photocatalysis involves interfacial electron transfer from the Ti^{4+} *d*-electron–derived conduction band to electrophilic molecules, and attack of surface hydroxyls by the O^{2-} *p*-electron–derived valence band holes (*15*). Interfacial electron transfer from photoexcited dye molecules into the conduction band of TiO_2, which is thought to occur on <10-fs time scales, initiates redox cycles in dye-sensitized photovoltaic cells (*10*–*12*, *16*). However, despite the presence of chemisorbed water as reactant or spectator, its role in charge transfer through metal oxide interfaces has not been explored by experiment or theory.

Here, we report a time-resolved two-photon photoemission (TR-2PP; Fig. 1) and density functional theory (DFT) study of wet electrons on H_2O/TiO_2(110) rutile surfaces. A wet-electron state 2.4 ± 0.1 eV above the Fermi level (E_F) is observed by excitation with 3.05-eV light of electrons from partially reduced terminal pentacoordinate $Ti_{5c}^{+4-\delta}$ ion sites only when both OH and H_2O are chemisorbed on TiO_2. Pump-probe measurements give a lifetime of 15 fs for the decay of electrons from the wet-electron surface state to the conduction band of TiO_2.

All experiments were carried out under ultrahigh vacuum (base pressure $<1 \times 10^{-10}$ mbar). The surface electronic structure is explored for the stoichiometric and hydroxylated H_2O/TiO_2 surfaces. Stoichiometric TiO_2(110)-(1×1) surfaces were prepared by cycles of Ar^+ sputtering and annealing in O_2 atmosphere (3×10^{-7} mbar) as described in (*20*). Annealing the stoichiometric surfaces at 900 K in vacuum for 30 min introduces surface bridging O vacancies (Fig. 1B) (*18*, *21*). Thus, reduced surfaces were hydroxylated by exposure to distilled and degassed H_2O at 100 K (*22*–*24*). The sample was excited with 3.05-eV photons delivered in pulses of 10-fs duration and 1.7-nJ energy at 90-MHz repetition rate (*20*). 2PP spectra were measured with a hemispherical electron-energy analyzer (*20*). Interferometric two-pulse correlation (I2PC) measurements of the electron dynamics were recorded for fixed photoelectron energies by scanning the delay between identical pump-probe pulses (*25*).

[1]Department of Physics and Astronomy, [2]Department of Chemistry, University of Pittsburgh, Pittsburgh, PA 15260, USA. [3]Hefei National Laboratory for Physical Sciences at Microscale, University of Science and Technology of China, Hefei, Anhui 230026, China.

*To whom correspondence should be addressed. E-mail: petek@pitt.edu

Typical 2PP spectra of the stoichiometric and reduced TiO_2(110) surfaces before and after exposure to 1.3 Langmuir (1 L = 1.33×10^{-6} mbar·s) of H_2O (Fig. 2), span the range from the work function to the maximum energy (~6.1 eV) given by the two-photon absorption from E_F. The O vacancies introduce excess charge, which is distributed over several Ti_{5c}^{4+} ions to form a broad density of states (DOS) with a maximum 0.9 eV below E_F (*19*, *26*, *27*). With 3.05-eV photons, 2PP was excited exclusively from this $Ti^{+4-\delta}$ DOS even for the nominally stoichiometric surfaces (Fig. 1A). Adsorption of H_2O on the stoi-

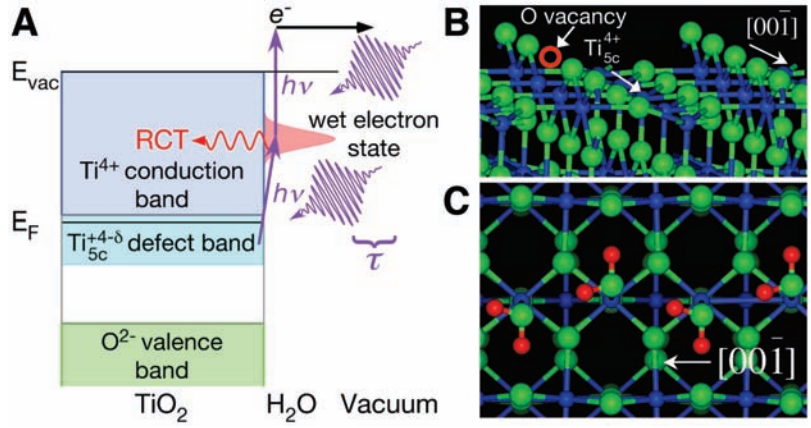

Fig. 1. (**A**) The schematic diagram for the detection of wet-electron states by 2PP spectroscopy. Electrons are excited by two-photon absorption (indicated in purple) from $Ti_{5c}^{+4-\delta}$ defect states to above the work function (E_{vac}). The analysis of photoemitted electron energy with respect to the Fermi level (E_F) yields 2PP spectra representing the density of occupied and unoccupied states. 2PP is resonance enhanced on hydroxylated TiO_2 surfaces by the wet-electron state at 2.4 eV. Measurement of the wet-electron state decay by resonant charge transfer (RCT) is performed by scanning the delay τ between pump and probe excitation pulses (*hν*). (**B**) The calculated structure of the TiO_2(110) surface. Bridging oxygen (green) rows align along the [001] crystallographic direction. The red circle indicates a bridging O vacancy, which is the most common defect on reduced TiO_2(110) surfaces. Acidic pentacoordinate Ti_{5c}^{4+} (blue) sites bind O atoms of water molecules. (**C**) The calculated structure of H_2O/TiO_2 for 1-ML coverage. Hydrogen bonding tilts the bridging O atoms and H_2O toward each other. Red spheres indicate H atoms.

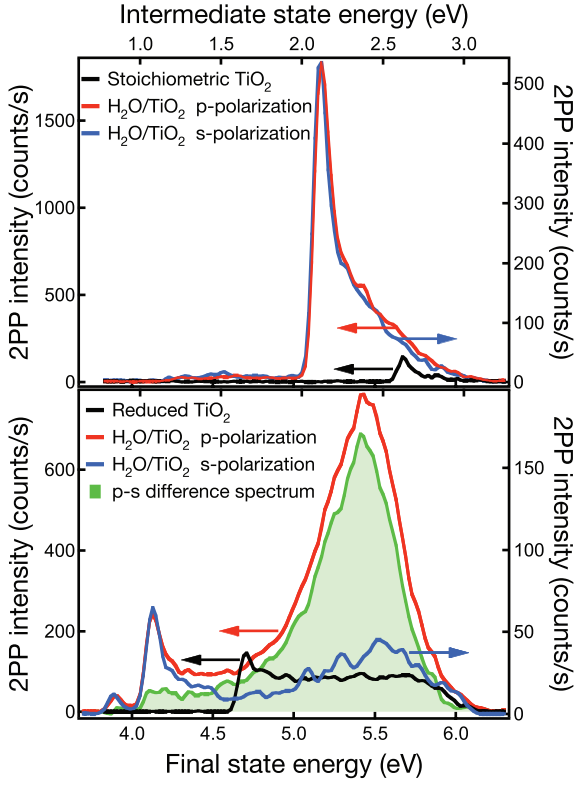

Fig. 2. 2PP spectra of the (**top**) stoichiometric and (**bottom**) reduced TiO_2 surfaces before and after deposition of ~1 ML of H_2O. The H_2O/TiO_2 spectra are taken with s- and p-polarized light. The s-polarized spectra are expanded 3× to normalize the intensities at the work-function edge (horizontal arrows indicate the appropriate axis for each spectrum). The difference between thus normalized p- and s-polarized spectra (green) for the reduced surface isolates the additional DOS of the wet-electron state. The final-state energy is that measured for photoelectrons with respect to E_F, whereas the intermediate-state energy is later reduced by the 3.05-eV photon energy.

chiometric TiO_2 surfaces transfers some charge to the $Ti^{+4-\delta}$ DOS as deduced by the work-function decrease; however, the profiles for the 2PP spectra with p- and s-polarized excitation are identical (Fig. 2, top) (*20*). With the higher O vacancy defect density, the reduced TiO_2 surfaces have a lower work function and higher $Ti^{+4-\delta}$ DOS than the stoichiometric surfaces (*20*). However, when 2PP was excited by p-polarized light, adsorption of H_2O onto reduced surfaces introduces a new band, which was isolated in the difference spectrum in Fig. 2, bottom. Because it appears only in p-polarized 2PP spectra, and not in conventional ultraviolet photoemission spectra (UPS), we attribute this band to an intermediate unoccupied state 2.4 ± 0.1 eV above E_F with the transition moment normal to the surface (*20*, *23*, *25*). On the basis of the chemisorption properties of H_2O and DFT calculations described below, we identified the 2.4-eV band with wet-electron states.

The nature of chemisorption of H_2O on TiO_2 has been studied by temperature-programmed desorption (TPD), vibrational spectroscopy, UPS, and scanning tunneling microscopy (STM). H_2O molecules on reduced surfaces dissociate at bridging O vacancies by a diffusion-limited process at <135 K to form two uncorrelated bridging OH species (*22–24*, *26*, *28*). After titrating the vacancies, water adsorbs molecularly at Ti^{4+}_{5c} ion sites between the bridging O rows up to 1-monolayer (ML) coverage (Fig. 1C) (*22*). Because the interaction of H_2O with the amphoteric oxide surface is stronger than with other H_2O molecules, the first monolayer molecules are aligned in a 2D structure (*22*) (Fig. 1C). Beyond the first monolayer, the second monolayer is disordered and the structure of bulk H_2O develops from the third monolayer.

We considered the assignment of the wet-electron state based on its dependence on adsorption of both H_2O and OH. The marked difference between the 2PP spectra of H_2O/TiO_2 in Fig. 2 is caused by a few percent (<5%) of H_2O molecules that dissociate to form OH on reduced surfaces (*29*). The wet electron–state intensity (integrated peak area) also depends on the H_2O exposure (Fig. 3A). The resonance intensity is maximum for 1.35 L of water and saturates at ~25% of its maximum value above 3 L. According to our modeling of the work function change, which is also shown in Fig. 3A, the exposure of 1.35 L corresponds to ~1-ML H_2O coverage (*20*).

To confirm that the wet-electron state attains maximum intensity at 1 ML of H_2O, we measured 2PP spectra for surfaces where H_2O coverage was defined by surface temperature. TPD spectra of H_2O/TiO_2 surfaces, which measure the partial pressure of H_2O as the surface is heated at a constant rate, exhibit peaks at 155 and 270 K, respectively, for the desorption of water from the multilayer and monolayer films. Hydroxyl recombination to form H_2O leads to an additional peak at 500 K for hydroxylated surfaces (*22*, *26*). After dosing 3.7 L of H_2O onto a reduced surface, we measured 2PP spectra at several temperatures, and in Fig. 3B, we plot for each temperature the excess DOS arising from the wet-electron state. The peak intensity increased to a maximum at 180 K after multilayer H_2O present at 100 and 140 K desorbed to expose the first monolayer. The wet-electron DOS was nearly extinguished when the remaining H_2O desorbed at 300 K, confirming that the resonance maximum occurs for ~1-ML coverage. With only OH remaining on the surface at 300 K, a weak feature, which appears to be the low-energy wing of a peak that exists above 3.05 eV, remained. We conclude that the existence of wet-electron state at 2.4 eV requires the cooperative interaction between OH and H_2O on TiO_2.

Finally, we studied the wet-electron lifetimes by recording I2PC scans for reduced TiO_2 surfaces after different exposures to H_2O. In Fig. 4, we plot I2PC scans averaged over the optical phase and their fit to an optical Bloch equation model (*25*). All measurements were only weakly dependent on the intermediate-state energy; however, the adsorption of H_2O noticeably increases the intermediate-state lifetime. The I2PC scan for the bare surface was identical to the pulse autocorrelation, indicating that the 2PP process occurs via virtual intermediate states (*25*). The wet-electron lifetimes increased to 10 ± 1 and 14 ± 1 fs for exposures of 0.7 and 1.6 L of H_2O, respectively, and saturated at ~15 fs for >1-ML coverage. Because their energy relaxation is unlikely to be so fast, wet electrons probably decay by resonant charge transfer into the conduction band of TiO_2. Because the lifetime corresponds to only two periods of O-H stretching vibration, the nuclear motion of H_2O molecules is too slow to stabilize the wet-electron state in a more favorable hydration structure.

To assign the wet-electron state to specific adsorbate structures, we performed plane-wave pseudopotential DFT calculations for associatively chemisorbed H_2O at Ti^{4+}_{5c} sites and H adsorbed on bridging O sites of TiO_2 for various coverages and structures (*30–35*). The calculated distribution of orbitals for the lowest energy adsorbate-localized unoccupied states for 1 ML H_2O + 0.5 ML H, and 1-ML H structures, respectively, at 2.4 and 1.5 eV are shown in Fig. 5. The unoccupied states of the adsorbate-covered surfaces are either associated with the Ti^{4+} ions, which form the conduction band of TiO_2, or dangling H atoms on OH and H_2O. For each H_2O and H coverage and structure, we found unoccupied adsorbate-localized states, where the DOS is

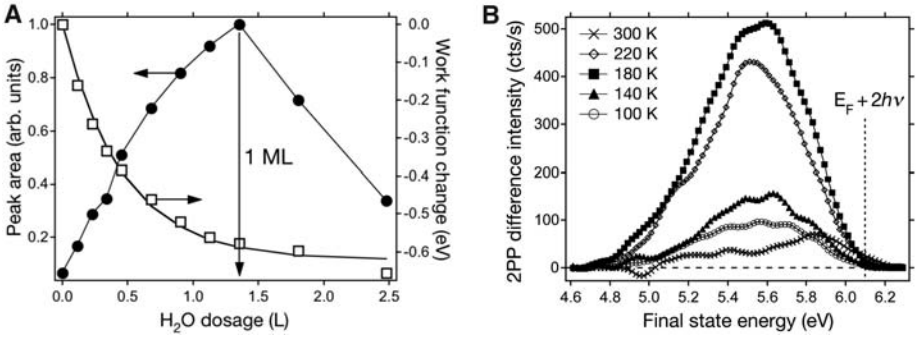

Fig. 3. (**A**) Plot of the wet electron–state peak area from difference spectra such as in Fig. 2, bottom (circles), and work-function change (squares) plotted as a function of water exposure. The solid line is a fit of the work-function change as described in (*20*). The coverage of 1.35 L for the intensity maximum and work-function saturation corresponds to the approximately 1-ML H_2O. The horizontal arrows indicate the appropriate axis for each measurement. (**B**) The difference spectra recorded at different temperatures after exposing the reduced TiO_2 to 3.7 L of H_2O at 100 K. Based on published TPD spectra, 1-ML coverage of H_2O is attained at 180 K where the wet-electron state has maximum intensity. Only OH remains above 300 K (*22*).

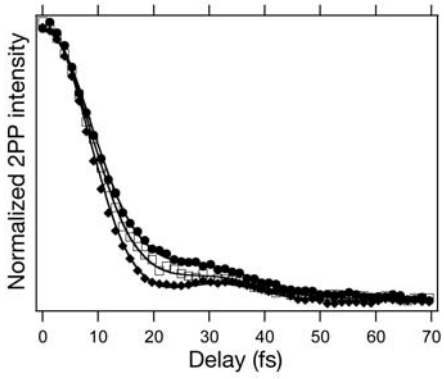

Fig. 4. Phase-averaged I2PC scans for the reduced TiO_2 (solid diamonds), and after exposure to 0.7 (open squares) and 1.6 L (solid circles) of H_2O. The lines represent fits with a three-level optical Bloch equation model with the use of experimentally measured pulse autocorrelation and assuming single exponential decay kinetics for the intermediate state (*25*). The bare surface intermediate-state lifetime is too short to measure, and 10 ± 1 and 14 ± 1 fs for 0.7 and 1.6 L H_2O/TiO_2, respectively.

concentrated on clusters of several dangling H atoms (Fig. 5A). The lowest unoccupied adsorbate-localized state energy correlates with the number of dangling H atoms in each cluster (Fig. 5C).

The association of electrons with the dangling H atoms is well known from the studies of hydrated electrons in water (*3*) and in water clusters (*4*–*9*). Based on the analogy to small water clusters where electrons are partially hydrated on cluster surfaces, we attribute the observed water-induced resonances to the partially hydrated wet-electron states that we calculated for TiO_2 surfaces. The ideal wet-electron structures investigated in Fig. 5 can explain the observed features of the experimentally studied heterogeneous surfaces. Notably, the lowest energy unoccupied state at 1.5 eV for 1 ML of H (Fig. 5B) consists of 1D-delocalized bands on bridging OH groups. When H_2O molecules are added to this structure, hydrogen bonding tilts the OH from surface normal and disrupts the optimal 1D structure. These structural changes reduce the surface dipole and the extent of electron delocalization, thereby increasing the energy of wet-electron states. The most relevant structure to our experiment is 1 ML H_2O + 0.5 ML H in Fig. 5A. For this structure, intervening bridging O atoms hinder orbital overlap between OH species to constrain electron delocalization to clusters involving single OH with two or more H_2O molecules (Fig. 5A). These clusters, which are representative of low-OH ($\ll$0.5 ML) coverage surfaces produced by our methods (*36*), have a calculated unoccupied level at 2.4 eV in good agreement with the experiment. Structures with two or more adjacent OH, which should have lower wet-electron energy, may occur with low probability and could be responsible for the characteristic low-energy tail in the difference spectrum in Fig. 2, bottom. Moreover, the calculated wet electron–state energy of 3.5 eV for 1 ML H_2O explains why the resonance cannot be excited with 3.05-eV light for stoichiometric surfaces. Because H_2O stabilizes the wet-electron state on isolated surface OH species, when H_2O desorbs above 300 K the resonance energy increases above 3 eV. In support of the existence of OH-localized states, in STM experiments, resonant tunneling into OH for bias of $\geq$+2.5 V leads to the enhanced contrast and desorption of H atoms from TiO_2 (*36*). Above 1-ML coverage, the second-layer H_2O molecules partially consume the dangling H atoms (*22*), thereby reducing the wet-electron DOS.

Hydrated electrons have also been observed on metals (*37*, *38*). However, metals lack the distinct acidic and basic sites present in oxides that could align or even dissociate H_2O to form OH. Therefore, associatively chemisorbed water on metals grows in bilayer structures that occupy the maximum number of H atoms in a hydrogen-bonding network (*38*). There are few preexisting sites that stabilize electrons, and to eject electrons into bilayer structures requires excitation above 3.2 eV into the conduction band of water. The excess energy of these conduction electrons can be used to disrupt the hydrogen-bonding network to form pockets of dangling H atoms. Once trapped at such sites, electrons are stabilized with respect to charge transfer to the metal substrate and undergo further hydration, which is accompanied by a reduction of energy to <2.6 eV, on >100-fs time scales (*37*, *38*).

The existence of wet electrons as excited states on the OH- and H_2O-covered TiO_2 is notable because conditions exist to support similar states on all oxide surfaces in contact with water or humid atmosphere. Depending on specific features of different surfaces, such as structures that promote cooperative interactions, and the acidity of OH species, the energy of the wet electrons could be even lower than calculated for 1 ML OH on TiO_2. For large band gap materials, the wet-electron states could even be occupied. Because they represent the lowest energy pathway for electron transfer at the metal-oxide/aqueous interfaces, wet-electron states may play an important role in photocatalysis and photoelectrochemical energy conversion on TiO_2 and other oxides. For instance, the surface OH impurity formed by the dissociative chemisorption of dye molecules could mediate the astoundingly fast charge injection into TiO_2 by providing conduction pathways through wet-electron states (*10*–*12*). Indeed, interfacial trap states of unknown origin have been invoked to explain the comparable excited state quenching rates of dyes on ZrO_2 as for TiO_2, even though the conduction band of ZrO_2 is not energetically accessible (*13*). Delocalized electron states attributed to Si-OH and Si-H also have been imaged by STM with a bias of +2.6 eV on a hydroxylated Si(100) surface (*39*). Thus, it is likely that wet-electron states perform important but yet unknown functions, for instance, as charge-transfer promoters at transparent metal-oxide electrodes used in organic-molecule–based devices and as electron traps in conventional semiconductor devices.

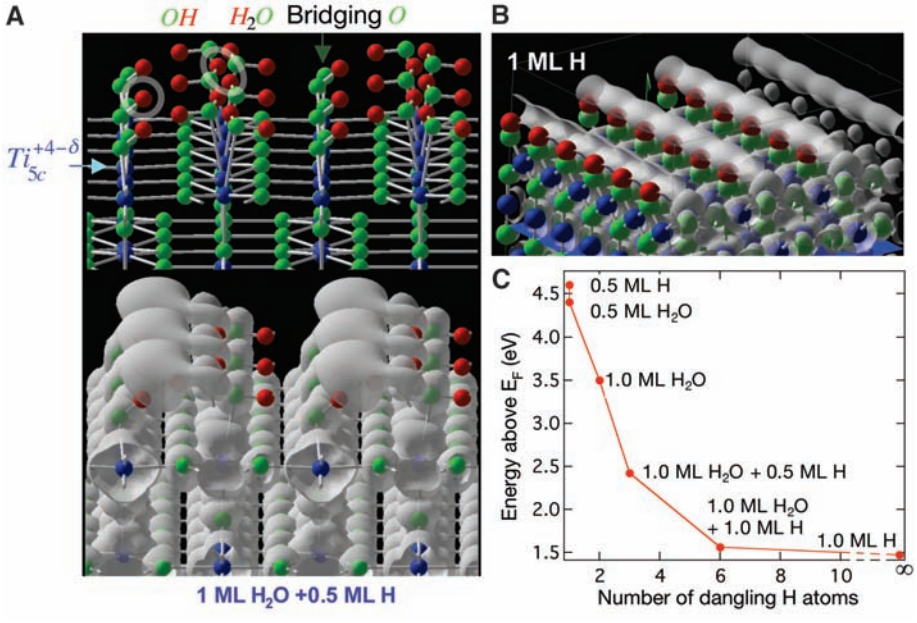

Fig. 5. (**A**) The optimized geometry of a TiO_2 surface covered with 1 ML H_2O + 0.5 ML H. The bottom panel shows the orbital distribution for the same structure at 2.4 eV above E_F. The adsorbate orbitals are delocalized in clusters involving one OH and one H atom each contributed by two adjacent H_2O molecules, which are indicated for a single cluster by white ellipsoids. (**B**) The optimized geometry and orbital distributions at 1.5 eV for 1 ML H on TiO_2. The hybridization of orbitals on H atoms into 1D chains along the bridging O rows makes this the most stable wet-electron state found by theory. (**C**) The correlation of the wet-electron energy for different coverages of H_2O and H adsorbates with the number of dangling H atoms in each hydration cluster. The infinite limit corresponds to the structure in (B). All calculated structures in the experimentally observable energy range are associated with clusters involving both OH and H_2O.

References and Notes

1. G. E. Brown Jr. *et al.*, *Chem. Rev.* **99**, 77 (1999).
2. L. Kevan, *Acc. Chem. Res.* **14**, 138 (1981).
3. J. Schnitker, P. J. Rossky, *J. Chem. Phys.* **86**, 3471 (1987).
4. K. S. Kim *et al.*, *Phys. Rev. Lett.* **76**, 956 (1996).
5. N. I. Hammer *et al.*, *Science* **306**, 675 (2004).
6. A. E. Bragg, J. R. R. Verlet, A. Kammrath, O. Cheshnovsky, D. M. Neumark, *Science* **306**, 669 (2004).
7. J. R. R. Verlet, A. E. Bragg, A. Kammrath, O. Cheshnovsky, D. M. Neumark, *Science* **307**, 93 (2005).
8. D. H. Paik, I.-R. Lee, D.-S. Yang, J. S. Baskin, A. H. Zewail, *Science* **306**, 672 (2004).
9. K. D. Jordan, *Science* **306**, 618 (2004).
10. C. Zimmermann *et al.*, *J. Phys. Chem. B* **105**, 9245 (2001).

11. J. Schnadt *et al.*, *Nature* **418**, 620 (2002).
12. N. A. Anderson and T. Lian, *Annu. Rev. Phys. Chem.* **56**, 491 (2005).
13. R. Huber, S. Spörlein, J. E. Moser, M. Grätzel, J. Wachtveitl, *J. Phys. Chem. B* **104**, 8995 (2000).
14. A. Fujishima, K. Honda, *Nature* **238**, 37 (1972).
15. M. R. Hoffmann, S. T. Martin, W. Choi, D. W. Bahnemann, *Chem. Rev.* **95**, 69 (1995).
16. A. Hagfeldt, M. Grätzel, *Acc. Chem. Res.* **33**, 269 (2000).
17. R. Wang *et al.*, *Nature* **388**, 431 (1997).
18. A. L. Linsebigler, G. Lu, J. T. Yates Jr., *Chem. Rev.* **95**, 735 (1995).
19. S. H. Szczepankiewicz, A. J. Colussi, M. R. Hoffmann, *J. Phys. Chem. B* **104**, 9842 (2000).
20. K. Onda, B. Li, H. Petek, *Phys. Rev. B* **70**, 045415 (2004).
21. U. Diebold, *Surf. Sci. Rep.* **48**, 53 (2003).
22. M. A. Henderson, *Surf. Sci.* **355**, 151 (1996).
23. I. M. Brookes, C. A. Muryn, G. Thornton, *Phys. Rev. Lett.* **87**, 266103 (2001).
24. R. Schaub *et al.*, *Phys. Rev. Lett.* **87**, 266104 (2001).
25. H. Petek, S. Ogawa, *Prog. Surf. Sci.* **56**, 239 (1997).
26. M. A. Henderson, W. S. Epling, C. H. F. Peden, C. L. Perkins, *J. Phys. Chem. B* **107**, 534 (2003).
27. J. Leconte, A. Markovits, M. K. Skalli, C. Minot, A. Belmajdoub, *Surf. Sci.* **497**, 194 (2002).
28. M. A. Henderson, *Surf. Sci. Rep.* **46**, 1 (2002).
29. To confirm that both H_2O molecules and OH are essential, we hydroxylated the stoichiometric surface, which does not exhibit the resonance when exposed to H_2O, with H atoms from a thermal cracking source (*36*). As anticipated, the dissociation of H_2O at bridging O vacancies and the reduction of bridging O atoms by gas phase H atoms (*40*) provide two alternative protocols for the detection of the wet-electron state.
30. The calculations with the Vienna ab Initio Simulation Package code use the generalized gradient approximation with the spin-polarized Perdew-Wang exchange-correlation functional. The oxygen 1*s* and Ti 1*s* to 3*p* are treated as core states. We use the projector augmented-wave (PAW) potential, which is generally more accurate than the ultrasoft pseudopotential. The surface is modeled by periodically repeated slabs containing three Ti layers separated by 10 Å vacuum gaps. A Monhkorst-Pack grid of $(3\times3\times1)$ *k* points is used for the (1×2) surface unit cell. Molecules are adsorbed on both sides of the slab to avoid formation of a dipole moment. The positions of all atoms are allowed to relax until the force acting on each is less than 0.02 eV $Å^{-1}$. We use a 400-eV plane-wave cutoff for the optimization and a 520-eV cutoff for the static calculation of the electronic structure.
31. G. Kresse, J. Hafner, *Phys. Rev. B* **47**, 558 (1993).
32. G. Kresse, J. Hafner, *Phys. Rev. B* **48**, 13115 (1993).
33. G. Kresse, J. Hafner, *Phys. Rev. B* **49**, 14251 (1994).
34. J. P. Perdew, Y. Wang, *Phys. Rev. B* **45**, 13244 (1992).
35. G. Kresse, J. Joubert, *Phys. Rev. B* **59**, 1758 (1999).
36. S. Suzuki, K. Fukui, H. Onishi, Y. Iwasawa, *Phys. Rev. Lett.* **84**, 2156 (2000).
37. C. Gahl, U. Bovensiepen, C. Frischkorn, M. Wolf, *Phys. Rev. Lett.* **89**, 107402 (2002).
38. C. Gahl *et al.*, *Surf. Sci.* **532-535**, 108 (2003).
39. M. Chander, Y. Z. Li, J. C. Patrin, J. H. Weaver, *Phys. Rev. B* **48**, 2493 (1993).
40. B. Li *et al.*, data not shown.

41. This work was supported by the U.S. Department of Defense Multidisciplinary University Research Initiative program under grant DAAD19-01-1-0619, and New Energy Development Organization of Japan "Molecular wire" project. The apparatus for TR-2PP was developed with support from NSF grant DMR-0116034. We thank J. T. Yates Jr. and his group for invaluable discussions.

4 January 2005; accepted 21 March 2005
10.1126/science.1109366

Deterministic Coupling of Single Quantum Dots to Single Nanocavity Modes

Antonio Badolato,[1]* Kevin Hennessy,[1]* Mete Atatüre,[3] Jan Dreiser,[3] Evelyn Hu,[1,2] Pierre M. Petroff,[1,2] Atac Imamoğlu[3]†

We demonstrate a deterministic approach to the implementation of solid-state cavity quantum electrodynamics (QED) systems based on a precise spatial and spectral overlap between a single self-assembled quantum dot and a photonic crystal membrane nanocavity. By fine-tuning nanocavity modes with a high quality factor into resonance with any given quantum dot exciton, we observed clear signatures of cavity QED (such as the Purcell effect) in all fabricated structures. This approach removes the major hindrances that had limited the application of solid-state cavity QED and enables the realization of experiments previously proposed in the context of quantum information processing.

Cavity QED experiments, where single atoms are strongly coupled to single cavity modes, have culminated in the demonstration of conditional quantum dynamics (*1*), quantum nondemolition measurement of photons, and creation of entanglement between three distinguishable quantum systems (*2*). The realization of such systems in the solid state, although challenging, offers several advantages (*3*). Indeed, a monolithically integrated cavity QED system consisting of a self-assembled quantum dot (QD) embedded within a nanocavity could have vanishing uncertainty in the relative location of the emitter with respect to the cavity electric field maxima and could allow for much stronger emitter-cavity coupling because of the ultrasmall cavity volumes. A number of experiments have already demonstrated the potential of QD-based solid-state cavity QED in applications such as single-photon sources (*4*–*6*). Nonetheless, because it is very difficult to predetermine the exact resonance energy and location of an optically active QD, all of the prior QD-based cavity QED experiments relied on a random spectral and spatial overlap between QDs and cavity modes (*7*–*9*). The difficulty in tuning the resonance energy of a fabricated nanocavity and the reduced likelihood of spatial overlap for the ultrasmall cavities of interest have so far limited the application of these solid-state cavity QED nanostructures. We demonstrate a deterministic approach to the QD nanocavity coupling based on two crucial components: (i) a positioning technique that allows us to locate a single QD at an electric field maximum of a photonic crystal (PC) nanocavity with 25-nm accuracy, and (ii) a precise spectral tuning of the cavity mode into resonance with any given QD emission line. This deterministic QD cavity coupling yields a spontaneous emission rate enhancement (Purcell effect) of the QD luminescence in all four fabricated devices.

Our basic material was a semiconductor heterostructure (Fig. 1A) grown by molecular beam epitaxy (*10*). The emitter-cavity system comprised free-standing PC membranes fabricated in a 180-nm layer of GaAs (*10*) with coherently embedded QDs. The square-lattice PC pattern with a single missing hole (S1) fabricated in the GaAs membrane can support a nondegenerate donor-type mode with a high quality factor (Q) and an ultrasmall mode volume (*11*).

The first key ingredient of our approach was the active positioning of a QD within the PC defect that eliminated the uncertainty in the relative position of the QD with respect to the cavity mode. We grew six vertically strain-correlated InAs/GaAs QD layers (*12*, *13*) in the GaAs membrane (Fig. 1A, right). The emission energy of the first QD layer (seed QD) was blue-shifted by in situ annealing the QDs when partly capped with GaAs (*14*). Five successive as-grown QD layers (stacked QDs) were stacked up to the surface (*15*), forming a tracer for the seed QD that was detectable by scanning electron microscopy (SEM). By resolving the location of a QD on the surface, we were able to determine the location of the seed QD that was of interest for coupling to a nanocavity. A matrix of gold markers was fabricated on the low-density QD region ($\approx 2 \times 10^5$ cm^{-2}) to map the isolated QDs relative to this matrix. With the use of electron beam lithography, we wrote the S1-PC pattern offset by the appropriate distance from the markers (*16*). The small white dot in Fig. 1B shows the SEM trace of the surface QD in one of our four devices (device I), which was positioned within 25 nm from one of the four

[1]Department of Electrical and Computer Engineering, [2]Materials Department, University of California, Santa Barbara, CA 93106, USA. [3]Institute of Quantum Electronics, ETH-Hönggerberg, CH-8093 Zürich, Switzerland.

*These authors contributed equally to this work.
†To whom correspondence should be addressed. E-mail: imamoglu@phys.ethz.ch